ACADEMIC PRESS

Available online at www.sciencedirect.com
SCIENCE DIRECT®

Journal of Catalysis 213 (2003) 151–162

JOURNAL OF CATALYSIS

www.elsevier.com/locate/jcat

The morphological evolution of the $Bi_2Mo_3O_{12}(010)$ surface in air–H_2O atmospheres

Svetlana V. Yanina and Richard L. Smith *

Department of Materials Science and Engineering, Massachusetts Institute of Technology, Cambridge, MA 02139, USA

Received 16 April 2002; revised 20 September 2002; accepted 26 September 2002

Abstract

Atomic force microscopy (AFM) has been used to examine the morphological evolution of the $Bi_2Mo_3O_{12}(010)$ surface at 400–600 °C in dry air and air–2.3% H_2O. The (010) cleavage surface is characterized by atomically flat terraces separated by straight steps that are integer multiples of $b/2$ (5.75 Å) in height. During treatments at or above 500 °C, the surface is etched due to the volatilization of Mo. In dry air, etching affects both steps and flat terraces and results in step recession, the development of half-unit-cell ($b/2$) step loops (pits and islands), and the accumulation of Bi-rich surface deposits. In air–2.3% H_2O, steps are etched with preference to terraces, and this leads to step recession as well as the formation of Bi-rich deposits. Mo volatilization proceeds at an enhanced rate in air–2.3% H_2O and culminates in the nucleation and growth of Bi_2MoO_6 and $Bi_2Mo_2O_9$ precipitates at 500 and 600 °C, respectively.

Keywords: Molybdate; Scanning probe microscopy; Partial oxidation; Volatilization; Molybdenum oxide

1. Introduction

Bismuth molybdates have been the subject of numerous investigations related to their ability to catalyze the selective oxidation and ammoxidation of alkenes [1–12]. While industrial catalysts are usually complex multicomponent molybdates, most research has focused on the simpler binary oxides of the Bi_2O_3–MoO_3 system, particularly $Bi_2Mo_3O_{12}$ (also known as α-bismuth molybdate), $Bi_2Mo_2O_9$ (β-bismuth molybdate), Bi_2MoO_6 (γ-bismuth molybdate), and their mixtures [1–6]. As a result of these studies, a considerable amount is known about the bulk structures of the individual compounds as well as the overall mechanisms of partial oxidation over them [6]. Comparatively little is known, however, about the surface structures of the bismuth molybdates and, as a result, the role surface structure plays in their reactivity [7]. These uncertainties motivated this atomic force microscopy (AFM) study of the $Bi_2Mo_3O_{12}(010)$ surface and its evolution during treatments in air and air–2.3% H_2O.

The results of bulk structural studies have generally indicated that $Bi_2Mo_3O_{12}$ is stable at elevated temperatures ($T \leqslant 500$ °C) in air and under conditions typical for the selective oxidation of alkenes [8–11]. At the same time, investigations with local bulk and surface-sensitive probes have shown that the structure and composition near $Bi_2Mo_3O_{12}$ surfaces can depart from that of the bulk. For example, using in situ transmission electron microscopy (TEM), Gai [13,14] observed the formation of a phase similar to $Bi_2Mo_2O_9$ (as well as Bi and MoO_3) within minutes at ~ 440 °C in propene and propene–O_2 (1 : 1) atmospheres. The $Bi_2Mo_2O_9$-like precipitates grew with reaction time and extended into the $Bi_2Mo_3O_{12}$ bulk, but they were unstable outside of the reducing environment of the in situ TEM cell [13]. X-ray photoelectron spectroscopy (XPS) analyses of calcined $Bi_2Mo_3O_{12}$ powders have generally indicated near-surface Bi/Mo ratios similar to that expected based on the bulk stoichiometry (i.e., Bi/Mo $\sim 2/3$), but ratios near unity have been observed in $Bi_2Mo_3O_{12}$–Bi_2MoO_6 mixtures and in nonstoichiometric $Bi_2Mo_3O_{12}$ (excess Bi) and Bi_2MoO_6 (excess Mo) [7,8,15,16]. Matsuura and coworkers [15] attributed this shared surface chemistry to a common surface layer similar to $Bi_2Mo_2O_9$, but alternate explanations based on surface oxide mixtures with an average Bi/Mo ~ 1 have also been advanced [17,18]. In a more

* Corresponding author.
E-mail address: smithrl@mit.edu (R.L. Smith).
URL address: http://web.mit.edu/smithrl/www/.

0021-9517/02/$ – see front matter
PII: S0021-9517(02)00024-6

recent XPS study, Briand and co-workers [19] reported surface enrichment of Mo (Bi/Mo ~ 0.55) in co-precipitated $Bi_2Mo_3O_{12}$ powders that had been calcined at 500 °C. Based on reactions with a probe molecule (methanol), the authors deduced that $Bi_2Mo_3O_{12}$ surfaces are largely composed of MoO_x species, in the form of a two-dimensional overlayer, due to spontaneous spreading similar to that observed when oxide supports are mixed with MoO_3 [19–21].

While XPS and TEM have provided some insight into the chemistry and phase composition near the surfaces of $Bi_2Mo_3O_{12}$ particles, little is known about the structure and morphology of the individual surfaces that actually bound the particles [7]. Furthermore, the structures and morphologies of these surfaces are expected to change during reactions at elevated temperatures, in response to a variety of thermochemical stimuli. Understanding these details of surface structure and dynamics is important because they bear directly on the population and configurations of surface sites and, therefore, reactivity. The objectives of this study were to characterize the structure of the $Bi_2Mo_3O_{12}(010)$ surface and its evolution during treatments in dry air and air–2.3% H_2O between 400 and 600 °C. This has been accomplished through a combination of atomic force microscopy (AFM), X-ray diffraction (XRD), and X-ray photoelectron spectroscopy (XPS) experiments on single crystal cleavage surfaces.

The (010) surface of $Bi_2Mo_3O_{12}$ was the focus of study for a number of reasons. $Bi_2Mo_3O_{12}$ crystallites are characteristically platy with large (010) and $(0\bar{1}0)$ faces and, as a result, these faces compose a significant fraction of the total surface areas of powdered samples. From a more practical experimental standpoint, $Bi_2Mo_3O_{12}$ crystals are readily cleaved normal to $\langle 010\rangle$, making it possible to easily and reproducibly prepare fresh (010) surfaces of bulk stoichiometry. Although bismuth molybdate catalysts are typically used at or below 500 °C, they are sometimes processed (i.e., calcined) above this temperature. For this reason, studies beyond normal operating temperatures were undertaken. Water vapor is of course normally present during calcining treatments as well as during selective oxidation reactions, at the least as a byproduct, and it is known to enhance the volatility of Mo [22–30]. Our results demonstrate that this volatility plays a central role in the evolution of the structure and chemistry of the $Bi_2Mo_3O_{12}(010)$ surface during thermal treatments.

2. Methods

2.1. $Bi_2Mo_3O_{12}$ crystal growth

The (010)-oriented $Bi_2Mo_3O_{12}$ single crystal plates ($\sim 5 \times 4 \times 1\ mm^3$) used in this study were cleaved from larger samples grown by flux and directional solidification approaches [31,32]. The plates were optically transparent and had a yellow hue. In a typical flux growth, 200–300 g of a 78% MoO_3 (99+%, Aldrich)–22% Bi_2O_3 (99%, Aldrich) molar mixture was first melted at 710 °C in an Al_2O_3 crucible. After 5 h at 710 °C, the melt was cooled slowly (0.5 °C/h) to 600 °C and then more rapidly (~ 20 °C/h) to room temperature. The solidified product consisted of a crumbly mixture of $Bi_2Mo_3O_{12}$ and MoO_3 crystals from which $Bi_2Mo_3O_{12}$ plates up to 1.5 cm on edge could be separated. In the directional solidification approach, crystals were grown by slowly cooling a MoO_3–25% Bi_2O_3 melt across a temperature gradient in a horizontal tube furnace. The growths were conducted in quartz tubes (i.d. = 13 mm) and yielded irregular boules (3–4 cm in length) composed of several $Bi_2Mo_3O_{12}$ crystals/grains.

2.2. Surface treatments

$Bi_2Mo_3O_{12}$ single crystals were treated in a continuous flow of the desired gas phase in a quartz reaction tube (length = 1 m, i.d. = 2.5 cm). Prior to treatment, fresh (010) and $(0\bar{1}0)$ surfaces were formed by cleavage with a razor blade in the ambient. Typically, 3–4 crystals were cleaved in half to yield 3–4 pairs of opposing (010) and $(0\bar{1}0)$ surfaces. The terminations of the $Bi_2Mo_3O_{12}(010)$ and $(0\bar{1}0)$ cleavage surfaces were not, at the outset, expected to be equivalent. Based on our observations, however, they appear to be related in a simple manner, which will be elaborated in Section 2.1. Following cleavage, the crystals were immediately placed in a high-purity Al_2O_3 boat and loaded into the reaction tube. The tube was then doubly purged by alternately evacuating with an oil-less pump and backfilling with the gas mixture of interest. A continuous gas flow of 100 $cm^3\,min^{-1}$ at 1 atm pressure was then established. The samples were subsequently heated to the desired reaction temperature (400–600 °C) in a horizontal split-tube furnace. It took less than 10 min to reach this temperature, and the actual temperature did not exceed the desired temperature by more than 1% throughout the thermal cycle. Temperature was monitored externally with a thermocouple that was positioned in contact with the reaction tube, directly adjacent to the samples.

The $Bi_2Mo_3O_{12}$ samples were treated for predetermined periods of time between 2 and 300 h. The principal atmospheres investigated were dry air (BOC) and air saturated with H_2O at 24 ± 1 °C ($\sim 2.3\%$ H_2O). The dry air was used as received and had an H_2O content of less than 10 ppm. The air–2.3% H_2O mixture was prepared by passing the dry air through two fritted H_2O bubblers connected in series. Following reaction, the samples were quickly cooled to room temperature under a flow of the test gas. Cooling was hastened by lifting the reaction tube out of the furnace. By doing so, it took less than 5 min for the samples to cool to below 200 °C, a temperature where prolonged treatments had no discernible (with AFM) effect on the $Bi_2Mo_3O_{12}(010)$ surface.

2.3. Surface characterization

Once the samples had cooled to room temperature, they were removed from the reaction tube and the exposed (010) and $(0\bar{1}0)$ surfaces were immediately characterized using atomic force microscopy (AFM) (Digital Instruments, Santa Barbara, CA) in the ambient. The surfaces were examined over the course of several hours, and at least three areas on four different crystals were studied. There were no perceptible (with AFM) changes in surface structure over the analysis period or even over extended (several days) exposures to the ambient. The AFM observations were made in the contact mode using Si_3N_4 probes with V-shaped cantilevers and pyramidal tips. The vertical calibration of the AFM scanner was checked periodically using steps on cleaved $MoO_3(010)$ surfaces as standards [33,34].

X-ray diffraction (XRD) was used to characterize the phase composition of treated single crystal surfaces. The (010) and/or $(0\bar{1}0)$ surface layers of the single crystals were selectively sampled, either by scraping the surfaces with a razor blade or by extraction with adhesive tape. Due to the small quantities of material available, the XRD samples were mounted on glass slides using double-sided adhesive tape. XRD analysis was performed on a θ–θ diffractometer (Rigaku, Tokyo, Japan) using Cu-K_α radiation supplied by a rotating anode generator operated at 60 kV and 300 mA. In some cases, parallel XRD experiments were also conducted with coarse $Bi_2Mo_3O_{12}$ powders ($\sim$ 0.25 g). The starting powders were prepared by crushing single crystals with an Al_2O_3 mortar and pestle.

X-ray photoelectron spectroscopy (XPS) (AXIS Ultra, Kratos Analytical, Manchester, UK) was used to probe the chemical compositions of cleaved and treated $Bi_2Mo_3O_{12}(010)$ surfaces. Of particular interest was the relative composition of Bi and Mo near the surface (i.e., the atomic Bi/Mo ratio). Following the desired treatments, the single crystals were immediately transferred to the load-lock of the XPS unit. Subsequently, XPS analysis was performed using monochromatized Al-K_α radiation. For any particular treatment condition, three or four different single crystal surfaces were analyzed. In the results section, the range of Bi/Mo ratios measured on the surfaces are reported. To enhance the surface sensitivity, the XPS samples were tilted ($\sim 70°$) for analysis. Following XPS, the samples' surface morphologies were characterized with AFM.

3. Results

3.1. The structure of the $Bi_2Mo_3O_{12}(010)$ and $(0\bar{1}0)$ cleavage surfaces

The morphologies of $Bi_2Mo_3O_{12}(010)$ and $(0\bar{1}0)$ cleavage surfaces were indistinguishable. Both were characterized by atomically flat terraces separated by straight steps (see Fig. 1). The distribution of steps across cleaved surfaces varied. Some regions had step populations similar to those depicted in Fig. 1, while others presented singular flat terraces as large as 100×100 μm^2, the upper limit of the AFM scanner. Cleavage surfaces exhibited two limiting step

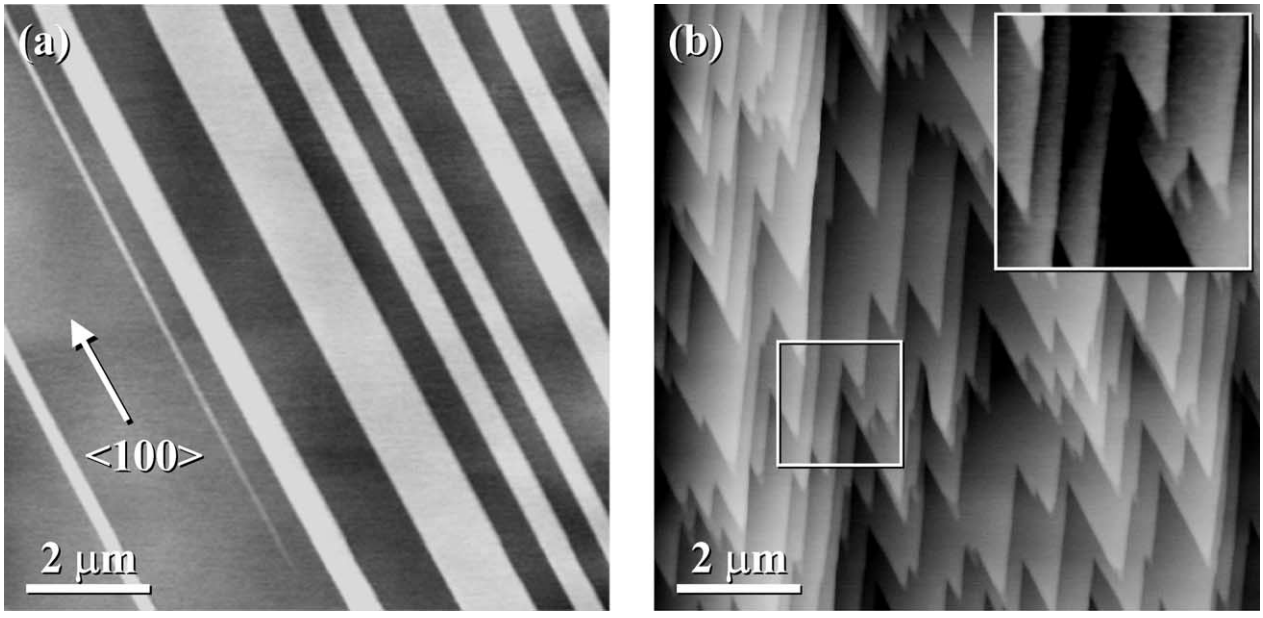

Fig. 1. Topographic AFM images of the limiting step morphologies on $Bi_2Mo_3O_{12}(010)$ and $(0\bar{1}0)$ cleavage surfaces. (a) Straight steps with edges parallel to ⟨100⟩ and heights that are an integer multiple of $b/2$. (b) Serrated terraces characteristically bounded by half-unit-cell steps accompanied by small triangular terraces (inset) bounded by quarter-unit-cell steps. The black-to-white contrasts in (a) and (b) correspond to topographic ranges of approximately 30 and 80 Å, respectively.

morphologies that, along with singular terraces, could usually be found in multiple regions on any particular surface. Most often, terraces were bounded by straight steps that extended for hundreds of micrometers along ⟨100⟩, as shown in Fig. 1a. The heights of these steps were invariably an integer multiple of 5.8 ± 0.5 Å, which corresponds to one-half of the b lattice parameter of $Bi_2Mo_3O_{12}$ ($b/2 = 5.75$ Å) [12]. In most cases, straight steps parallel to ⟨100⟩ were single-unit-cell steps (height $= b = 11.5$ Å).

Terraces with a triangular or serrated morphology were also formed during cleavage (see Fig. 1b). These terraces were characteristically bounded by half-unit-cell steps (height $= b/2$), but they were often accompanied by smaller triangular terraces bounded by quarter-unit-cell steps (height $= b/4$). The $b/4$-steps/terraces were localized at the protruding tips of the serrated terraces and usually extended less than 400 nm before transitioning to half-unit-cell steps (inset of Fig. 1b). During the course of study, multiple regions on at least 20 different cleavage surfaces were characterized, and steps whose heights were not an integer multiple of $b/2$ were only observed in the vicinity of serrated terraces. Even in areas with high densities of these terraces, as in Fig. 1b, terraces bounded by $b/4$-steps composed less than 1% of the total (010) terrace area. XPS analysis of (010) and $(0\bar{1}0)$ cleavage surfaces indicated near-surface compositions consistent with the bulk stoichiometry of $Bi_2Mo_3O_{12}$ (i.e., Bi/Mo $= 2/3 = 0.667$). Six cleavage surfaces from different crystals were analyzed, and all exhibited Bi/Mo ratios between 0.65 and 0.68.

The crystal structure of $Bi_2Mo_3O_{12}$ (space group $= P2_1/c$) has been described by Van Den Elzen and Rieck [12] and can be viewed as a distorted Scheelite with ordered Bi vacancies. The structure contains three distinct Mo sites, each of which is nominally coordinated by five O. In each case, four of the Mo–O bonds are short (1.68 to 1.91 Å), while the fifth is considerably longer (> 2.13 Å). As a result, the Mo coordination is usually regarded as tetrahedral [12–15]. There are two Bi sites. Each has four close O neighbors (at distances of 2.12 to 2.34 Å) and four that are much further away (2.61 to 2.94 Å). The Bi and Mo are concentrated in layers parallel to (010) that intersect b at approximately 1/8, 3/8, 5/8, and 7/8 (see Fig. 2a). Adjacent layers are bridged and held together by metal–oxygen, primarily Bi–O, bonds. (010) cleavage is expected to occur between these cation layers at one or more of the planes that intersect b at $\sim 1/4, 1/2, 3/4$, and 1. The fact that XPS data indicate a Bi/Mo ratio $\sim 2/3$ is consistent with this expectation, since each cation layer has a Bi/Mo ratio of 2/3. Due to the 2_1 screw axis along ⟨010⟩, the planes at 1/4 and 3/4 are equivalent, though rotated 180°with respect to one another. The planes at 1/2 and 1 are related in the same manner, but they are not equivalent to those at 1/4 and 3/4. Thus, there are two potential cleavage systems, 1/2–1 and 1/4–3/4, each composed of equivalent planes separated by $b/2$.

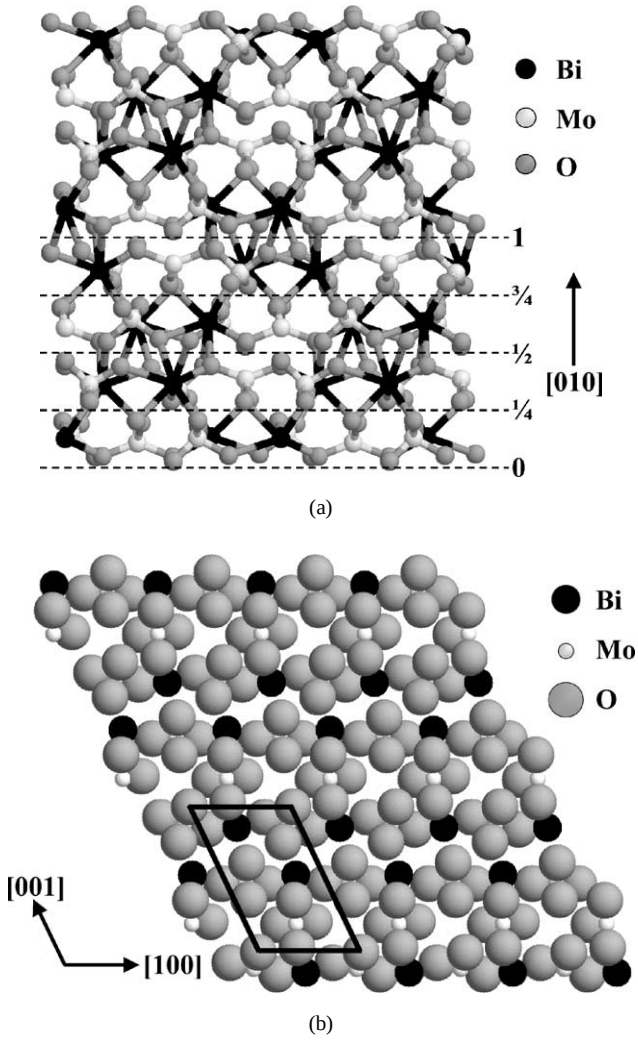

Fig. 2. (a) Bonding model of the $Bi_2Mo_3O_{12}$ structure viewed along ⟨100⟩ with the potential cleavage planes indicated. In this representation, the Mo coordination is assumed to be tetrahedral, while that of Bi is assumed to be eightfold. (b) Ionic space-filling model of the bulk terminated $Bi_2Mo_3O_{12}(010)$ surface formed through cleavage at the 1/2–1 system. In this representation, the radius of O^{-2} is assumed to be 1.4 Å. For clarity, the radii of Bi^{+3} and Mo^{+6} have been slightly exaggerated to 1.1 and 0.6 Å, respectively.

Although there are two viable cleavage systems, our AFM observations indicate that cleavage is dominated by one system. This is because steps that were not an integer multiple of $b/2$ (the distance between equivalent planes in each cleavage system) in height were encountered in only small populations during AFM studies. Furthermore, when such steps (i.e., the $b/4$-steps) were encountered, they were localized and extended less than 400 nm before transitioning to half-unit-cell ($b/2$) steps. Taken together, these characteristics point to a single, dominant cleavage system. Consequently, the terraces on cleaved $Bi_2Mo_3O_{12}(010)$ surfaces will, with the exception of the small population bounded by $b/4$-steps, have the same atomic termination. Note, however,

that the terminations of terraces separated by steps that are an odd multiple of $b/2$ will be rotated 180° with respect to one another. Terraces on $(0\bar{1}0)$ will be related in the same manner, but their termination will differ from that on (010), as will be described shortly.

While AFM observations indicate that cleavage is dominated by one cleavage system, they do not allow us to distinguish between the two candidates. Consideration of the bonding across the cleavage planes does, however, permit distinction. 1/2–1 cleavage would nominally require breaking fewer bonds than 1/4–3/4 cleavage. For each unit cell cleaved, resulting in the creation of opposing (010) and $(0\bar{1}0)$ surface cells, eight Bi–O and two Mo–O bonds would be broken across 1/2 or 1, while eight Bi–O and four Mo–O bonds would be broken across 1/4 or 3/4. In both systems however, the broken Mo–O bonds are associated with the fifth, distant O (Mo–O > 2.13 Å) around each Mo. These bonds are presumably broken easily, leaving the tetrahedral coordination of Mo intact. A clear distinction between the cleavage systems is evident when the Bi–O bonding is considered. The bonds broken at 1/2–1 are on average longer and, therefore, expected to be weaker than those at 1/4–3/4. All eight of the Bi–O bonds at 1/2–1 can be viewed as long and weak, with lengths of 2.60 to 2.79 Å. In contrast, cleavage at 1/4–3/4 would require breaking a number of short Bi–O linkages. Four are long (2.67 to 2.94 Å), but the other four are much shorter (2.22 to 2.24 Å). Hence, cleavage is favored at the 1/2–1 system. In the rare instances where terraces bounded by $b/4$-steps occurred, cleavage must have also propagated along the 1/4–3/4 system for short distances. With the identification of the cleavage system, a model for the bulk-terminated $Bi_2Mo_3O_{12}(010)$ surface can be proposed (see Fig. 2b). Based on the bonding arguments outlined above, Mo at the surface is tetrahedrally coordinated by O, while each Bi has two dangling bonds. Cleavage at 1/4–3/4 would yield similar coordination environments, except the broken Bi–O bonds would be shorter.

As noted earlier, the terminations of the opposing (010) and $(0\bar{1}0)$ cleavage surfaces are expected to be different. The cleavage plane that intersects b at 1 (and 1/2) contains a center of inversion. Therefore, the crystal elements across the plane are related through the combination of a mirror and a 180° rotation, and the terminations of (010) and $(0\bar{1}0)$ are mirror images. They are, however, nonsuperimposable mirror images (i.e., enantiomers), because their respective surface cells are oblique (plane group = P1). Though unfavorable, cleavage at 1/4–3/4 would also lead to enantiomorphic surfaces, because the cleavage plane coincides with the c glide plane in the $Bi_2Mo_3O_{12}$ structure. Since only relatively weak bonds are ruptured during cleavage, surface reconstructions that might destroy the enantiomorphic relationship between (010) and $(0\bar{1}0)$ are not anticipated [33–37]. Regardless, the opposing surfaces will be related by a mirror and would be expected to behave identically in achiral environments, such as air–H_2O [38]. Through this study, differences were not observed in their cleavage structures, as noted earlier, or in their behavior during treatments in dry air and air–2.3% H_2O. Therefore, we will simply refer to the (010) and $(0\bar{1}0)$ collectively as (010) through the remainder of the text.

3.2. Evolution of $Bi_2Mo_3O_{12}(010)$ in air–H_2O ($T \leqslant 500$ °C)

The $Bi_2Mo_3O_{12}(010)$ cleavage surface was not modified in any manner detectable with AFM during dry air anneals in excess of 100 h at 400 °C. Within 2 h at 500 °C, morphological changes were apparent, and surfaces were marked by irregularly shaped islands and pits with lateral dimensions less than 300 nm (see Fig. 3a). The heights of the islands above (and pits below) adjacent terraces varied, even across any particular one of these features, but ranged from 3 to 6 Å ($\sim b/4$–$b/2$). Due to the general roughness of the surfaces, it was often difficult to identify the transitions from distinct islands (or pits) to terraces [39]. While the region in Fig. 3a principally contained islands, pits were prominent in other areas, indicating that the $Bi_2Mo_3O_{12}(010)$ surface was eroded or etched during the treatment. This etching was nonspecific, as terraces and steps were affected with essentially equal probability. The morphologies of (010) surfaces treated for 4 h at 500 °C in dry air were not significantly different from those of surfaces treated for 2 h. XPS analysis of surfaces treated for 4 h indicated a slight increase in the Bi concentration (relative to the cleavage surface); the Bi/Mo ratios of the surfaces all fell between 0.69 and 0.74.

In contrast to surfaces treated in dry air, $Bi_2Mo_3O_{12}(010)$ surfaces treated in air–2.3% H_2O were altered during treatments at 400 °C. These surfaces also exhibited morphological changes consistent with erosion or etching, but the etching was specific, as only steps were affected. Etching was initially evident in the "rounding-off" of the protruding tips of serrated terraces and in the absence of the associated $b/4$-terraces that were observed on cleavage surfaces (Fig. 1b). This rounding was confined to within ~ 500 nm of the terrace tips after 48 h at 400 °C. Etching was accelerated at 500 °C, and changes in step morphology were apparent after only 2 h (see Fig. 3b). These changes included rounding of the step tips as well as step recession (advance of a step toward its upper terrace). Flat (010) terraces appeared unchanged after 2 h in air–2.3% H_2O at 500 °C and were indistinguishable from those on fresh cleavage surfaces. Surfaces treated for 4 h at 500 °C in air–2.3% H_2O exhibited similar step-specific etching. Despite the rather modest change in surface morphology during the treatment, XPS analysis indicated significant Bi enrichment near the surface. Three different surfaces were analyzed, and all exhibited Bi/Mo ratios between 0.76 and 0.80.

With extended reactions at 500 °C, morphological changes in the $Bi_2Mo_3O_{12}(010)$ surface were more pronounced. Within 48 h in dry air, the irregular islands and pits of variable height (Fig. 3a) gave way to micrometer-sized step

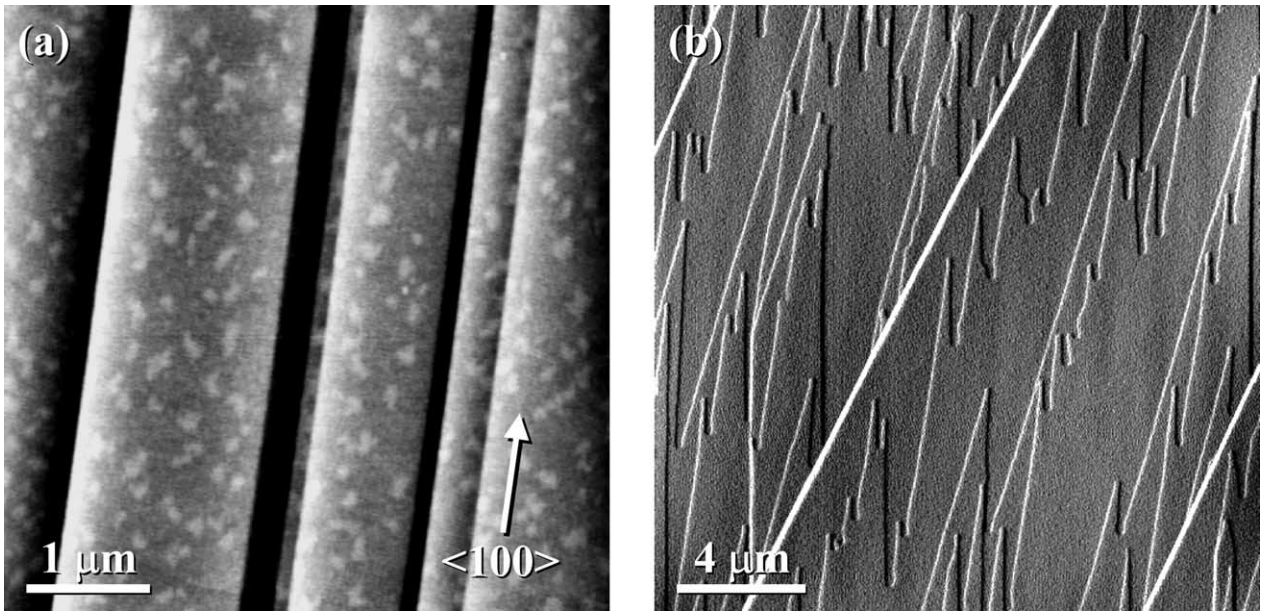

Fig. 3. (a) Topographic AFM image of a $Bi_2Mo_3O_{12}$(010) surface following treatment for 2 h at 500 °C in dry air. (b) AFM deflection image of a $Bi_2Mo_3O_{12}$(010) surface treated for 2 h at 500 °C in air–2.3% H_2O. The black-to-white contrast in (a) corresponds to a topographic range of 60 Å.

loops (islands) that were a uniform half unit cell ($b/2$) in height (see Fig. 4a). Islands persisted through treatments up to 120 h (the longest time investigated), but surface pits were only rarely observed. The (010) terraces that separated the islands were usually decorated with fine deposits 3–5 Å high that made the surfaces appear "grainy" in AFM images. Due to their small size, the lateral dimensions of these deposits could not be reliably assessed [39]. Etching at steps was also apparent (see Fig. 4b). Steps receded irregularly but as discrete units that were $b/2$ in height (i.e., as half-unit-cell steps). As a result, the straight steps characteristic of the cleavage surface were transformed into irregular half-unit-cell steps. Small deposits were also found in the vicinity of steps that had receded. The deposits were often aligned in rows along ⟨100⟩, most likely marking the positions of the receding steps at earlier points in time. Whether at steps or on flat terraces, etching in dry air at 500 °C led to an increase in the step density on $Bi_2Mo_3O_{12}$(010) as well as a complete change in step morphology, i.e., from straight to irregular and curved. XPS revealed that etching also resulted in a gradual increase in the surface Bi concentration with reaction time. Samples analyzed after 72 h at 500 °C in dry air exhibited Bi/Mo ratios of 0.72–0.76.

There was significant region-to-region variability in the morphology of $Bi_2MO_3O_{12}$(010) surfaces treated for extended periods at 500 °C in air–2.3% H_2O. This variability appeared to be influenced by the initial structure of the cleavage surface, in particular the density of steps. Following reactions of as long as 144 h, flat (010) terraces far ($\geqslant 10$ μm) from steps often appeared unmodified over areas as large as 50×50 μm^2. Intermittently, however, the terraces were interrupted by isolated pits and, with reactions in excess of 24 h, accompanying nanometer-scale deposits (see Fig. 4c). The pits were composed of half-unit-cell step loops and invariably encircled the deposits, which had heights of up to 20 Å after 72 h. While this pitting could only have resulted from local material loss, the loss was incongruent, since some matter was left behind in the surface deposits.

In contrast to flat terraces, steps were prone to modification and etching at 500 °C in air–2.3% H_2O. This resulted in step recession, once again as discrete half-unit-cell steps, as shown in Fig. 4d. The morphologies of adjacent steps often alternated from irregular and curved to comparatively straight. The straight steps were usually decorated with deposits that had heights of 20–40 Å after 72 h. This alternating step arrangement probably resulted from the dissociation of straight single-unit-cell steps (which were characteristic of the cleavage surface) into half-unit-cell steps, with the upper half receding while the lower remained in place. The steps receded in an irregular fashion and left surface deposits and, on some terraces, irregular half-unit-cell islands in their wake. This combination of step recession and deposit accumulation indicates, once again, that the $Bi_2Mo_3O_{12}$(010) surface is incongruently etched away at 500 °C. In many cases, deposits were located on terraces and islands bounded by receding steps, but far from the steps themselves. This suggests that steps had swept through these regions previously and, therefore, at least one $b/2$-thick layer of the surface had already been etched away.

Acicular precipitates were usually apparent within 72 h at 500 °C in air–2.3% H_2O and can be seen in Fig. 4d. These features had heights of 40–100 Å and were often oriented at an angle of $\sim 40°$ with respect to the $Bi_2Mo_3O_{12}$ ⟨100⟩ axis. The precipitates occurred in groups or clusters that were encompassed by pits. The pits were comprised of

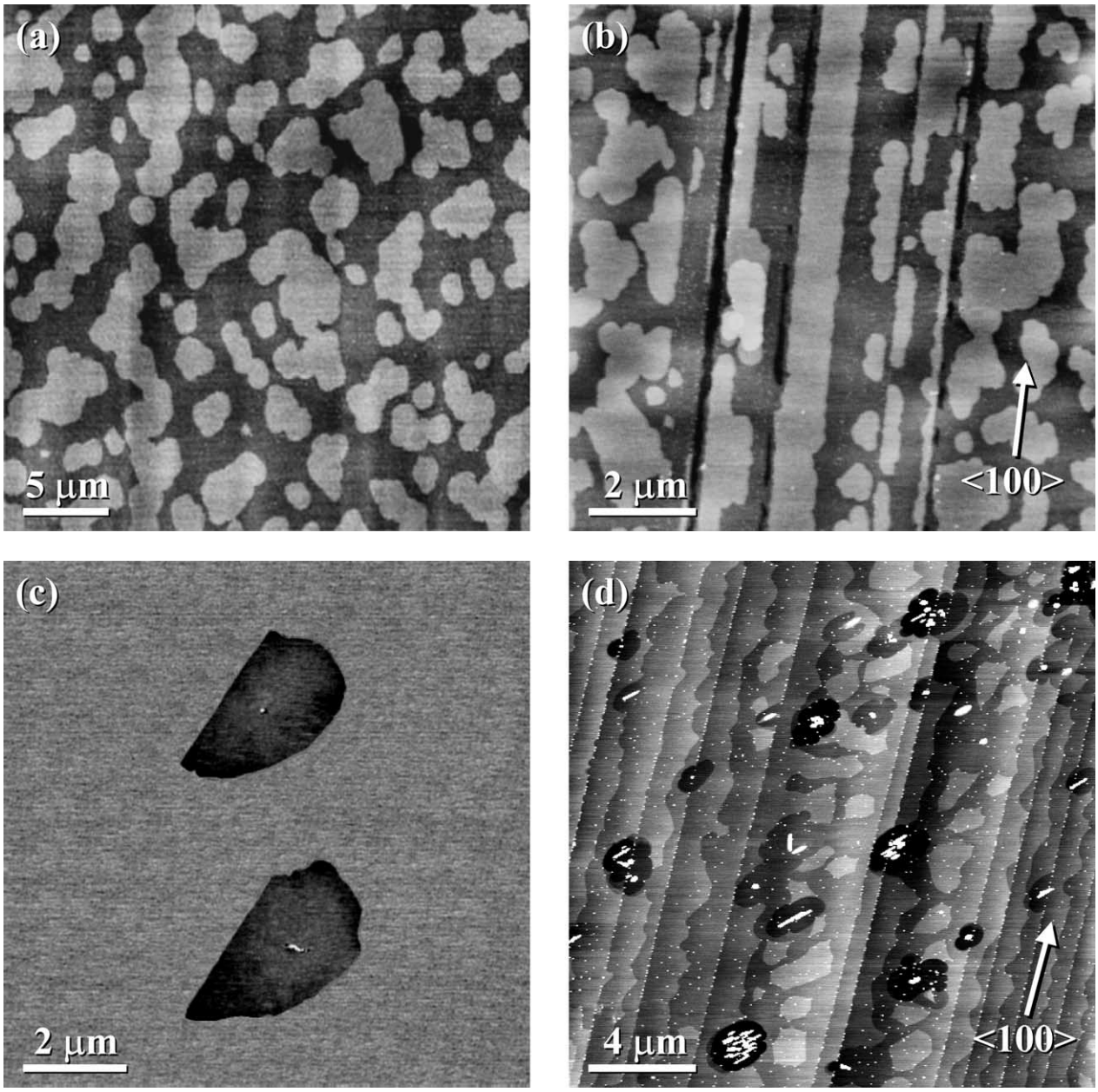

Fig. 4. Topographic AFM images of $Bi_2Mo_3O_{12}$(010) surfaces treated for 72 h at 500 °C in dry air (a) and (b) and air–2.3% H_2O (c) and (d). The black-to-white contrasts in (a)–(d) correspond to topographic ranges of 30, 60, 40, and 100 Å, respectively.

concentric half-unit-cell step loops and had depths of up to 6*b* (∼ 70 Å). In general, the widths and depths of the pits increased with the total volume of precipitates they enveloped. The surface deposits and the precipitates interacted differently with steps. Receding steps and islands often had sharp and discontinuous changes in their curvature. These discontinuities almost invariably coincided with the occurrence of surface deposits, indicating that the deposits pinned the steps and hindered their migration. In contrast, the acicular precipitates appeared to locally enhance step recession, particularly in directions away from the precipitates themselves.

Though areas such as those in Fig. 4c and 4d were common on $Bi_2Mo_3O_{12}$(010) surfaces treated in excess of 48 h at 500 °C in air–2.3% H_2O, the microstructures of the surfaces were dominated by a population of much larger precipitates, which had lateral dimensions of up to 25 μm after 72 h (see Fig. 5). The precipitates were embedded in the (010) surface but often had portions that rose above (50–100 nm) adjacent terraces. The distribution of these precipitates was easily studied using optical microscopy. The precipitates were generally dispersed uniformly across the (010) surfaces of treated crystals and occupied 20–30% (by

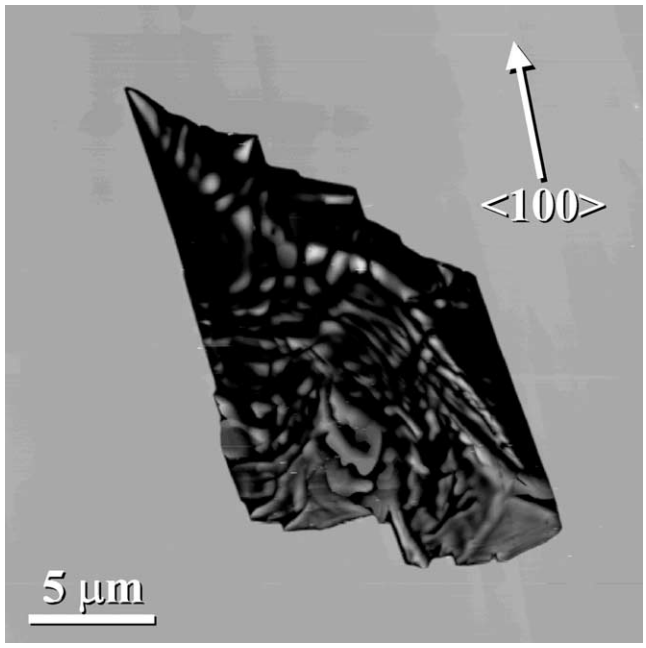

Fig. 5. Topographic AFM image of a precipitate formed on a $Bi_2Mo_3O_{12}$(010) surface during a 144-h treatment at 500 °C in air–2.3% H_2O. The precipitates developed into an overlayer within ∼ 250 h. XRD analysis of these overlayers demonstrated that the precipitates were γ-Bi_2MoO_6.

area) of the surfaces within 72 h. Enrichment was, however, usually evident near the edges of the crystals. The average size of the precipitates increased with reaction time, as did the fraction of the surface they covered, until a virtually continuous precipitate overlayer/coating developed within approximately 250 h at 500 °C. The overlayers were fragile and often delaminated and crumbled on cooling, which made it difficult to measure their thickness, but they were at most 10 μm thick (after 350 h).

X-ray diffraction (XRD) analysis of samples scraped from single crystal (010) surfaces treated for 200 and 350 h at 500 °C in air–2.3% H_2O revealed the presence of two crystalline phases, $Bi_2Mo_3O_{12}$ and γ-Bi_2MoO_6. Given the fact that micrometer-sized Bi_2MoO_6 precipitates developed within 48 h at 500 °C in air–2.3% H_2O, it is not surprising that XPS indicated enhanced Bi concentrations at (010) surfaces treated for or in excess of 48 h. For example, surfaces treated for 72 h exhibited Bi/Mo ratios of 0.85–0.96. It should, of course, be kept in mind that these XPS data only provide an indication of the average near-surface composition. Obviously, the local Bi/Mo ratio in regions with large Bi_2MoO_6 precipitates (as in Fig. 5) would be expected to exceed that in regions free of precipitates (Fig. 4c).

Parallel experiments with $Bi_2Mo_3O_{12}$ powders yielded results consistent with the single crystal studies. After 200 h at 500 °C in air–2.3% H_2O, three phases were detected in powder beds with XRD, $Bi_2Mo_3O_{12}$ and small amounts of Bi_2MoO_6 and MoO_3. During powder experiments, MoO_3 crystals were also deposited on the walls of the reaction tube where the flowing gas exited the furnace. Thus, both the $Bi_2Mo_3O_{12}$ single crystals and powders lost Mo through volatilization in air–2.3% H_2O at 500 °C. The nucleation and growth of a second phase (Bi_2MoO_6) richer in Bi indicates that the extent of Bi loss was small relative to that of Mo in air–2.3% H_2O. In dry air, on the other hand, secondary phases were not detected on (010) surfaces (via AFM or optical microscopy) or in powders (via XRD) treated for up to 120 and 250 h, respectively. Furthermore, there was no indication of MoO_3 (or other material) accumulation at the reactor exhaust. Hence, Mo and Bi volatility in dry air were both small compared to that of Mo in air–2.3% H_2O. Material was, however, still removed from the (010) surface during treatments in dry air, as evidenced by incongruent terrace etching and step recession, and the surface became enriched with Bi, indicating that the volatility of Mo in dry air was greater than that of Bi.

3.3. Evolution of $Bi_2Mo_3O_{12}$(010) in air–H_2O ($T = 600$ °C)

The modifications introduced to the $Bi_2Mo_3O_{12}$(010) surface at 600 °C were similar to those at 500 °C. Surfaces were again marked by incongruent etching and the array of accompanying morphological changes, including step recession, half-unit-cell step loops (pits and islands), and deposits. There were, however, some noteworthy differences. First, the rate at which these features developed was accelerated at the higher temperature. Additionally, the step morphology was more regular at 600 °C, as the edges of islands, pits, and receding steps were smooth, with an almost circular morphology. Finally, flat (010) terraces were etched to a greater extent at 600 °C, both in the presence and absence of H_2O. Terraces treated in dry air (see Figs. 6a and 7a) were uniformly modified after 2 h at 600 °C and were characterized by half-unit-cell step loops (pits and islands) and deposits with heights of up to 100 Å. Surfaces treated in air–2.3% H_2O exhibited more variability. The region in Fig. 6b is characteristic of terraces that eroded extensively over 2 h in air–2.3% H_2O. In other areas (see Fig. 7b), fewer pits and deposits were encountered, often at concentrations comparable to those observed at 500 °C.

Micrometer-sized precipitates were apparent after only 2 h at 600 °C on $Bi_2Mo_3O_{12}$(010) surfaces treated in either air–2.3% H_2O or dry air. The precipitates were uniformly distributed across the (010) surfaces, although enrichment near the edges of the crystals was again evident. The precipitates that developed in dry air were characteristically acicular and had lengths of up to 30 μm after 2 h (see Fig. 7a). The precipitates that formed in air–2.3% H_2O (see Fig. 7b) were more equiaxed and usually had lateral dimensions in excess of 150 μm. The image in Fig. 7b shows only one corner of a trapezoid-shaped precipitate that was more than 200 μm long. Irrespective of the atmosphere, XPS analysis indicated elevated Bi concentrations at $Bi_2Mo_3O_{12}$(010) surfaces treated for 2 h at 600 °C. Surfaces treated in dry air

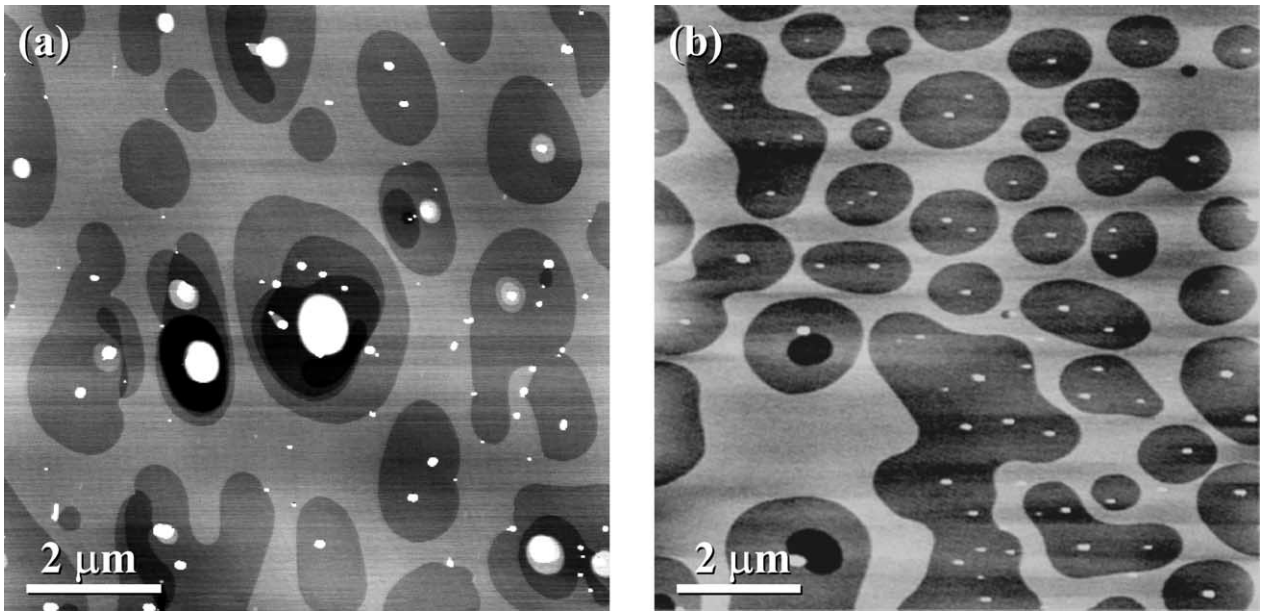

Fig. 6. Topographic AFM images of terraced regions on $Bi_2Mo_3O_{12}$(010) surfaces treated for 2 h at 600 °C in dry air (a) and air–2.3% H_2O (b). The black-to-white contrasts in (a) and (b) correspond to topographic ranges of 110 and 60 Å, respectively.

exhibited Bi/Mo ratios of 0.73–0.77, while those treated in air–2.3% H_2O had Bi/Mo ratios of 0.79–0.86. The precipitates grew rapidly in air–2.3% H_2O, and an overlayer developed within 24 h. XRD analysis of these overlayers revealed that the precipitate phase was β-$Bi_2Mo_2O_9$. This assignment was also supported by parallel powder experiments. After 24 h at 600 °C in air–2.3% H_2O, $Bi_2Mo_2O_9$ was easily detected with XRD. MoO_3 crystals were deposited at the reactor exhaust during both single crystal and powder treatments in excess of 24 h.

Precipitate growth was slow in dry air, and $Bi_2Mo_3O_{12}$(010) surfaces treated for up to 100 h at 600 °C did not yield enough of the precipitate phase for it to be identified with XRD. Similarly, phase changes were not detected in $Bi_2Mo_3O_{12}$ powders treated for up to 100 h at 600 °C in dry air. Energy dispersive X-ray analysis performed within

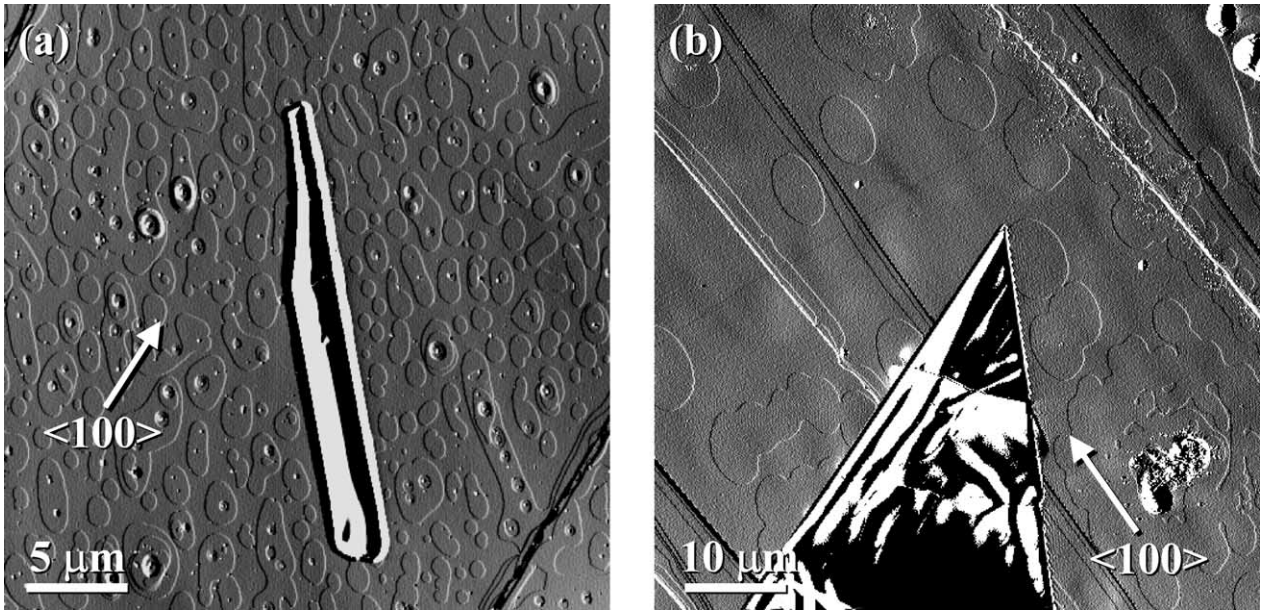

Fig. 7. AFM deflection images of precipitates formed on $Bi_2Mo_3O_{12}$(010) surfaces during 2-h anneals at 600 °C in dry air (a) and air–2.3% H_2O (b). In air–2.3% H_2O, the precipitates developed into an overlayer within ∼ 24 h. XRD analysis of these overlayers demonstrated that the precipitates were β-$Bi_2Mo_2O_9$.

a scanning electron microscope (SEM) indicated that the precipitates had a Bi/Mo stoichiometry close to 1/1, but the possibility that the underlying $Bi_2Mo_3O_{12}$ matrix contributed to the measured composition could not be ruled out. Hence, the precipitates were enriched in Bi but not necessarily $Bi_2Mo_2O_9$.

4. Discussion

The results of our AFM, XRD, and XPS experiments clearly demonstrate that $Bi_2Mo_3O_{12}$ loses Mo through volatilization above 500 °C in dry air and air–2.3% H_2O. Not surprisingly, this volatility leads to changes in the structure and chemistry of the (010) surface. The most conspicuous consequence of Mo loss is the precipitation of new Bi-rich bismuth molybdates, with Bi_2MoO_6 and $Bi_2Mo_2O_9$ forming in air–2.3% H_2O at 500 °C and 600 °C, respectively. Though Mo volatilization proceeds more slowly in dry air, Bi-rich precipitates are formed within only 2 h at 600 °C. The observation that H_2O enhances Mo volatility is of course not surprising, as it has been linked to Mo volatilization from Mo-containing alloys, silicides, and oxides alike [22–30]. This is usually attributed to the formation of volatile $MoO_2(OH)_2$ (g) through direct reaction with H_2O [22–30]. Although the present study has addressed more moderate temperatures and environmental conditions, the results are fully consistent with those of Zhang and co-workers [25], which showed that Bi volatilization from $Bi_2Mo_3O_{12}$ (as well as Bi_2MoO_6 and $Bi_2Mo_2O_9$) powders was negligible in dry (N_2) and humid (H_2O) atmospheres below ∼ 700 °C and that Mo volatilization was accelerated by H_2O.

That volatile Mo loss from $Bi_2Mo_3O_{12}$ in air–2.3% H_2O results in the precipitation of Bi_2MoO_6 at 500 °C and $Bi_2Mo_2O_9$ at 600 °C is in agreement with the Bi_2O_3–MoO_3 phase diagram proposed by Egashira and co-workers [9]. The formation of these phases indicates that $Bi_2Mo_3O_{12}$ is unstable under the conditions examined, undoubtedly due to the disparate volatilities of Mo and Bi. Our conclusion that $Bi_2Mo_3O_{12}$ is unstable is not necessarily inconsistent with the results of prior bulk studies, even though these studies have generally concluded that the phase is stable in air and under typical reaction conditions [8–17]. This is because the precipitates we observed on single crystal surfaces at comparable temperatures and over comparable durations (usually less than 100 h) would not have been detected in powders with bulk structural probes, such as XRD and Raman and infrared spectroscopies [8–17]. For example, Snyder and Hill [8] did not detect phase changes in $Bi_2Mo_3O_{12}$ powders with in situ Raman spectroscopy over 24 h at 600 °C in dry air. Similarly, we detected no changes with XRD over 100 h under the same conditions. Only through protracted anneals can sufficient volume fractions of the second phases be obtained to enable identification with XRD. Of course, decomposition and precipitation are initiated over much shorter periods (e.g., within 2 h at 600 °C), as are other significant changes in the structure and chemistry of the $Bi_2Mo_3O_{12}$(010) surface.

Within 2 h at or above 500 °C, the morphology of the $Bi_2Mo_3O_{12}$(010) surface is altered as a result of incongruent etching reactions that proceed in dry air and air–2.3% H_2O. In both atmospheres, etching is marked by the removal of material (step recession and/or surface pitting) and the accumulation of surface deposits. Given the dissimilar volatilities of Mo and Bi, surface pitting and step recession can be attributed to local Mo volatilization and the concomitant decomposition of $Bi_2Mo_3O_{12}$. Since Bi volatility is essentially negligible, decomposition/etching leaves the surface enriched in Bi, as verified with XPS. Initially, the residual Bi is likely present as surface adatoms, but it eventually condenses with O (and perhaps some Mo) to form the observed deposits. This mechanism is certainly consistent with the close spatial association between deposits and receding steps and pits on surfaces treated in both air–2.3% H_2O (Figs. 4c, d, and 6b) and dry air (Figs. 4b, 6a, and 7a). While the deposits are undoubtedly enriched in Bi, their exact chemical makeup is unclear. They may well be Bi_2MoO_6 or $Bi_2Mo_2O_9$ nuclei (depending on the temperature), but they could also be a metastable intermediate, which then reacts with $Bi_2Mo_3O_{12}$ or the Mo-rich vapor to form the precipitates.

One would expect there to be mechanistic differences between etching in the presence and absence of H_2O. For example, Mo volatilization is expected to proceed via MoO_3 in dry air, but as $MoO_2(OH)_2$ in air–2.3% H_2O [23,25]. This might in part account for the fact that etching primarily affects steps in air–2.3% H_2O, while both steps and terraces are etched in dry air. The formation and desorption (volatilization) of $MoO_2(OH)_2$ must presumably be preceded by H_2O adsorption, whereas MoO_3 desorption can proceed independent of an adsorption step. Therefore, the specificity of etching in air–2.3% H_2O might reflect a structural sensitivity of H_2O chemisorption. However, both MoO_3 and $MoO_2(OH)_2$ desorption should be favored at steps over terraces, since this requires breaking fewer bonds and circumvents the energy barrier associated with the nucleation of an isolated pit on a singular terrace (i.e., two-dimensional or layer-by-layer evaporation) [40–45].

The fact that flat (010) terraces are uniformly etched in dry air indicates that, at some point during the treatment, the vapor pressure of MoO_3 in the reactor is below that required for the onset of layer-by-layer evaporation [40–45]. Rather than a sustained nonspecific (layer-by-layer) process, etching could just proceed in a nonspecific manner early in the treatment. As the $Bi_2Mo_3O_{12}$ samples are first heated to the treatment temperature, the driving force (i.e., vapor undersaturation) for evaporation and pit nucleation is at its highest, since the initial vapor pressures of MoO_3 and Bi_2O_3 in the reactor are effectively zero. As the treatment progresses, the vapor pressures will rise and the driving force will be reduced, potentially to the point that pit nucleation is no longer feasible. Such a transition—from layer-by-

layer to step/defect-controlled evaporation—could explain the transition from small islands and pits of variable ($b/4$–$b/2$) height (Fig. 3a) to uniform half-unit-cell ($b/2$) islands (Figs. 4a and 4b) during treatments at 500 °C. Subsequently, the half-unit-cell islands must in fact erode preferentially from their bounding steps, since new surface pits are only rarely observed at long exposures. The change in surface morphology that accompanies the transition is probably indicative of coarsening of the initial (transient) morphology ($\sim$ 2 h, Fig. 3a) to a lower energy configuration ($\sim$ 72 h, Fig. 4a).

The rarity of terrace etching in air–2.3% H_2O indicates that the vapor pressure of MoO_3, which is related to the vapor pressure of $MoO_2(OH)_2$, is sufficiently high so that layer-by-layer evaporation is largely suppressed [40–45]. This behavior is somewhat counterintuitive because Mo volatilizes more rapidly in air–2.3% H_2O than in dry air, indicating that the driving force (vapor undersaturation) for pit nucleation should be greater in air–2.3% H_2O. The difference could however be explained if H_2O disproportionately enhances the rate at which Mo can volatilize from steps compared to terraces, for example by lowering the activation energy for desorption. Such a mechanism is consistent with the fact that steps are etched in air–2.3% H_2O at as low as 400 °C. Rapid volatilization from steps, defects (e.g., dislocations), and the crystal edges as the samples are heated to the treatment temperature could raise the pressure of MoO_3 to the point that layer-by-layer evaporation is not feasible. As the treatment temperature is increased, the vapor undersaturation required for layer-by-layer evaporation should decrease, consistent with the increased occurrence of pits on singular terraces in air–2.3% H_2O at 600 °C.

Although there are differences in the manner in which the $Bi_2Mo_3O_{12}(010)$ surface is etched in dry air and air–2.3% H_2O, the surface evolves to have similar morphological characteristics in the two environments. For example, Mo loss results in Bi enrichment and the development of Bi-rich deposits. While steps on the cleavage surface are characteristically straight, steps on treated surfaces are curved. Furthermore, steps are always an integer multiple of $b/2$ in height. Terraces bounded by smaller steps, resulting either from cleavage (Fig. 1b) or short exposures at 500 °C (Fig. 3a), are annealed out within 72 h at 500 °C. Recalling the symmetry and bonding arguments outlined with regard to cleavage (Section 3.1), this points to a consistent $Bi_2Mo_3O_{12}(010)$ termination. All the terraces on $(01\bar{0})$ will have the same ideal termination, while those on $(0\bar{1}0)$ will be a mirror image. We assume this is the same termination favored by 1/2–1 cleavage (Fig. 2b), as it affords the lowest possible broken bond density. Since Mo sites are generally thought to play a role in reactant chemisorption on bismuth molybdates, it is interesting to note that this terrace termination presents Mo that are tetrahedrally coordinated by O and effectively bond saturated. Hence, if coordinatively unsaturated Mo atoms are required for chemisorption, the reactivities of the (010) and $(0\bar{1}0)$ surfaces would be expected to be controlled by defects, such as steps and oxygen vacancies.

Acknowledgments

This work was supported by the Department of Materials Science and Engineering of the Massachusetts Institute of Technology (MIT). The authors gratefully acknowledge the technical assistance of Mr. J. Chen, Mr. R. Li, and Ms. L. Metzger and the use of the shared experimental facilities of the National Science Foundation—Materials Research Science and Engineering Center (NSF-MRSEC) at MIT.

References

[1] J. Haber, in: R. Grasselli, J. Brazdil (Eds.), Solid State Chemistry in Catalysis, American Chemical Society, Washington, DC, 1985, p. 1.
[2] D.A. Jefferson, J.M. Thomas, M.K. Uppal, R.K. Grasselli, J. Chem. Soc. Chem. Commun. 594 (1983).
[3] A.W. Sleight, in: A.K. Cheetham, P. Day (Eds.), Solid State Chemistry Compounds, Clarendon Press, Oxford, 1992, p. 166.
[4] D.J. Buttrey, D.A. Jefferson, J.M. Thomas, Philos. Mag. A 53 (1986) 897.
[5] P.N. Rylander, in: J.R. Anderson, M. Boudart (Eds.), Catalysis Science and Technology, Springer, New York, 1983, p. 2.
[6] T.P. Snyder, C.G. Hill Jr., Catal. Rev. Sci. Eng. 31 (1989) 43.
[7] N. Arora, G. Deo, I.E. Wachs, A.M. Hirt, J. Catal. 159 (1996) 1.
[8] T.P. Snyder, C.G. Hill Jr., J. Catal. 132 (1991) 536.
[9] M. Egashira, K. Matsuo, S. Kagawa, T. Seiyama, J. Catal. 58 (1979) 409.
[10] L.D. Krenzke, G.W. Keulks, J. Catal. 64 (1980) 295.
[11] J.F. Brazdil, D.D. Suresh, R.K. Grasselli, J. Catal. 66 (1980) 347.
[12] A.F. Van Den Elzen, G.D. Rieck, Acta Crystallogr. B 29 (1973) 2433.
[13] P.L. Gai, J. Solid State Chem. 49 (1983) 25.
[14] P.L. Gai, Catal. Rev. Sci. Eng. 34 (1992) 1.
[15] I. Matsuura, R. Schut, K. Hirakawa, J. Catal. 63 (1980) 152.
[16] D.A.G. Van Oeffelen, J.H.C. Van Hooff, G.C.A. Schuit, J. Catal. 95 (1985) 84.
[17] J. Kumar, E. Ruckenstein, J. Solid State Chem. 31 (1980) 41.
[18] D. Carson, G. Coundurier, M. Forissier, J.C. Vedrine, J. Chem. Soc. Faraday Trans. 79 (1983) 1921.
[19] L.E. Briand, A.M. Hirt, I.E. Wachs, J. Catal. 202 (2001) 268.
[20] I.E. Wachs, Catal. Today 27 (1996) 437.
[21] C.-B. Wang, Y. Cai, I.E. Wachs, Langmuir 15 (1999) 1223.
[22] T. Millner, J. Neugebauer, Nature 163 (1949) 601.
[23] G.R. Belton, A.S. Jordan, J. Phys. Chem. 69 (1965) 2065.
[24] T. Lim, S.W. Weller, J. Catal. 108 (1987) 175.
[25] L. Zhang, D. Liu, B. Yang, J. Zhao, Appl. Catal. A Gen. 117 (1994) 163.
[26] M.K. Meyer, A.J. Thom, M. Akinc, Intermetallics 7 (1999) 153.
[27] M. Akinc, M.K. Meyer, M.J. Kramer, A.J. Thom, J.J. Huebsch, B. Cook, Mater. Sci. Eng. A 261 (1999) 16.
[28] R.L. Smith, G.S. Rohrer, J. Catal. 163 (1996) 12.
[29] R.L. Smith, G.S. Rohrer, J. Catal. 180 (1998) 270.
[30] R.L. Smith, G.S. Rohrer, J. Catal. 184 (1999) 49.
[31] T. Chen, J. Cryst. Growth 20 (1973) 29.
[32] A. Grandin De l'eprevier, D.A. Payne, J. Cryst. Growth 51 (1981) 377.
[33] R.L. Smith, G.S. Rohrer, J. Solid State Chem. 124 (1996) 104.
[34] R.L. Smith, G.S. Rohrer, K.S. Lee, D.-K. Seo, M.-H. Whangbo, Surf. Sci. 367 (1996) 87.
[35] G.S. Rohrer, W. Lu, R.L. Smith, A. Hutchinson, Surf. Sci. 292 (1993) 261.

[36] T. Oshio, Y. Sakai, S. Ehara, J. Vac. Sci. Technol. B 12 (1994) 2055.
[37] C. Noguera, Physics and Chemistry at Oxide Surfaces, Cambridge Univ. Press, Cambridge, UK, 1996.
[38] C.F. McFadden, P.S. Cremer, A.J. Gellman, Langmuir 12 (1996) 2483.
[39] R.L. Smith, G.S. Rohrer, in: D.A. Bonnell (Ed.), Scanning Tunneling Microscopy and Spectroscopy: Theory Techniques and Applications, 2nd ed., VCH, New York, 2001.
[40] W.K. Burton, N. Cabrera, Discuss. Faraday Soc. 5 (1949) 33.
[41] W.K. Burton, N. Cabrera, Discuss. Faraday Soc. 5 (1949) 40.
[42] F.C. Frank, Discuss. Faraday Soc. 5 (1949) 48.
[43] J.P. Hirth, Acta Metall. 7 (1959) 755.
[44] J.B. Hudson, Surface Science: An Introduction, Wiley, New York, 1992.
[45] W.W. Mullins, G.S. Rohrer, J. Am. Ceram. Soc. 83 (2000) 214.